(1972); Y. I. Arshavsky *et al.*, *ibid.* **151**, 493 (1978).
28. D. J. Krupa, J. K. Thompson, R. F. Thompson, *Science* **260**, 989 (1993).
29. J. P. Welsh and J. A. Harvey, *J. Physiol. (London)* **444**, 459 (1991).
30. R. E. Clark, A. A. Zhang, D. G. Lavond, *Behav. Neurosci.* **106**, 879 (1992); G. A. Clark, D. A. McCormick, D. G. Lavond, R. F. Thompson, *Brain Res.* **291**, 125 (1984).
31. The proximity of FTNs to other VRNs makes it impossible to do this experiment with standard methods for either reversible or permanent ablation of neural tissue. The profound effect of lesions in the vestibular nucleus can be seen in T. Uemura and B. Cohen, *Acta Oto-Laryngol. Suppl.* **315**, 1 (1973).
32. R. E. Clark and D. G. Lavond, *Behav. Neurosci.* **107**, 264 (1993); P. F. Chapman, J. E. Steinmetz, L. L. Sears, R. F. Thompson, *Brain Res.* **537**, 149 (1990).
33. See (*29*). In contrast, reversible inactivation of the AIN with muscimol blocked acquisition of conditioning (*28*). However, this result may reflect the effects of residual activity in the presynaptic terminals in the nucleus; for further discussion, see (*15*).
34. A. E. Luebke and D. A. Robinson, *Exp. Brain Res.* **98**, 379 (1994).
35. A. M. Pastor, R. R. DeLaCruz, R. Baker, *J. Neurophysiol.* **72**, 1383 (1994).
36. A. M. Partsalis, Y. Zhang, S. M. Highstein, *ibid.*, **73**, 632.
37. M. Dufosse, M. Ito, P. J. Jastreboff, Y. Miyashita, *Brain Res.* **150**, 611 (1978); F. A. Miles, D. J. Braitman, B. M. Dow, *J. Neurophysiol.* **43**, 1477 (1980); E. Watanabe, *Brain Res.* **297**, 169 (1984); S. G. Lisberger, T. A. Pavelko, D. M. Broussard, *J. Neurophysiol.* **72**, 928 (1994); S. G. Lisberger, T. A. Pavelko, H. M. Bronte-Stewart, L. S. Stone, *ibid.*, p. 954.
38. J. E. Desmond and J. W. Moore, *Exp. Brain Res.* **65**, 59 (1986); R. F. Thompson *et al.*, *Physiol. Psychol.* **8**, 262 (1980); T. W. Berger, B. Alger, R. F. Thompson, *Science* **192**, 483 (1976).
39. M. D. Mauk and B. P. Ruiz, *Behav. Neurosci.* **106**, 666 (1992).
40. J. L. Raymond and S. G. Lisberger, *Soc. Neurosci Abstr.* **20**, 1194 (1994).
41. The VOR is measured as the eye movement response to a head turn in darkness to study the eye movements driven by vestibular stimulation in isolation from visually driven eye movements, which may contribute to the responses measured during head turns in the light.
42. Learned timing is expressed somewhat differently in the conditioned eyelid response and the VOR. When the tone CS and air-puff US are paired with a long interval, the learned eyelid response has no early component, whereas when the vestibular and image motion stimuli are paired with a long interval, the learned VOR response has both early and late components. When the tone CS and air-puff US are paired with a short interval, the learned eyelid response has no late component, whereas when the vestibular and image motion stimuli are paired with a short interval, the learned VOR response has both early and late components. These apparent differences may not reflect fundamental differences in the principles of operation of the two systems. Rather, they may reflect a difference in the resting discharge of neurons in the two circuits and the consequent difference in the threshold for the CS and the vestibular stimulus to elicit a behavioral response, or they may reflect small differences in the training protocols that have been used to induce learning in the two systems (for example, for pairing at a short interval, the vestibular stimulus continues after the end of the image motion stimulus, but the tone CS does not continue after the air-puff US).
43. M. Ito, *Annu. Rev. Neurosci.* **12**, 85 (1989); D. J. Linden, M. H. Dickinson, M. Smeyne, J. A. Connor, *Neuron* **7**, 81 (1991).
44. F. A. Miles and S. G. Lisberger, *Annu. Rev. Neurosci.* **4**, 273 (1981).
45. The simple-spike output of the cerebellum does not appear to contain information appropriate to guide learning under all conditions in which learning occurs, for example, when adapting with high-frequency sinusoidal stimuli [J. L. Raymond and S. G. Lisberger, *Soc. Neurosci. Abstr.* **21**, 139 (1995)].
46. F. Tempia, N. Dieringer, P. Strata, *Exp. Brain Res.* **86**, 568 (1991); N. H. Barmack and J. I. Simpson, *J. Neurophysiol.* **43**, 182 (1980).
47. D. A. McCormick, J. E. Steinmetz, R. F. Thompson, *Brain Res.* **359**, 120 (1985); C. H. Yeo, M. J. Hardiman, M. Glickstein, *Exp. Brain Res.* **63**, 81 (1986).
48. D. V. Buonomano and M. D. Mauk, *Neural Comput.* **6**, 38 (1994); H. L. Galiana, in *Adaptive Mechanisms in Gaze Control*, A. Berthoz and G. Melvill Jones, Eds. (Elsevier, Amsterdam, 1985), pp. 327–344; B. W. Peterson, J. F. Baker, J. C. Houk, in *Activity-Driven CNS Changes in Learning and Development, Ann. N.Y. Acad. Sci.* **627**, 319 (1991).
49. L. M. Optican and D. A. Robinson, *J. Neurophysiol.* **44**, 1058 (1980), L. M. Optican and F. A. Miles, *ibid.* **54**, 940 (1985); N. H. Donegan, R. W. Lowery, R. F. Thompson, *Soc. Neurosci. Abstr.* **9**, 331 (1983); N. F. Popov, in *Higher Nervous Activity*, D. S. Fursikov, M. O. Gurevisch, A. N. Zalmanzon, Eds. (Com. Acad. Press, Moscow, 1929), vol. 1, pp. 140–148; A. I. Karamian, V. V. Fanardijian, A. A. Kosareva, in *Neurobiology of Cerebellar Evolution and Development, First International Symposium*, R. Llinas, Ed. (American Medical Association, Chicago, 1969), pp. 639–673.
50. We thank the members of the Lisberger and Mauk laboratories and D. Buonomano for helpful comments on earlier versions of this paper. Supported by NIH grants EY03878 (S.G.L.), EY10198 (S.G.L.), and MH46904 (M.D.M.); Office of Naval Research contract N00014-94-1-0269 (S.G.L.); a NASA Research Associate Fellowship (J.L.R.); two McKnight Scholars Awards (M.D.M., S.G.L.); and a McKnight Development Award (S.G.L.).

RESEARCH ARTICLES

A "Schrödinger Cat" Superposition State of an Atom

C. Monroe,* D. M. Meekhof, B. E. King, D. J. Wineland

A "Schrödinger cat"–like state of matter was generated at the single atom level. A trapped $^9Be^+$ ion was laser-cooled to the zero-point energy and then prepared in a superposition of spatially separated coherent harmonic oscillator states. This state was created by application of a sequence of laser pulses, which entangles internal (electronic) and external (motional) states of the ion. The Schrödinger cat superposition was verified by detection of the quantum mechanical interference between the localized wave packets. This mesoscopic system may provide insight into the fuzzy boundary between the classical and quantum worlds by allowing controlled studies of quantum measurement and quantum decoherence.

Quantum mechanics allows the preparation of physical systems in superposition states, or states that are "smeared" between two or more distinct values. This curious principle of quantum mechanics (*1*) has been extremely successful at describing physical behavior in the microscopic world—from interactions of atoms with photons to interactions at the subnuclear level. But what happens when we extend the quantum superposition principle to macroscopic systems conventionally described by classical physics? Here, superpositions introduce a great amount of conceptual difficulty, as pointed out in 1935 by the celebrated Einstein-Podolsky-Rosen (*2*) and Schrödinger cat (*3*) paradoxes. For example, in Schrödinger's thought experiment (*3*), an unfortunate cat is placed in a quantum superposition of being dead and alive (correlated with a single radioactive atom that has and has not decayed). The state of the system can be represented by the entangled quantum mechanical wave function,

$$\psi = \frac{|\text{☺}\rangle|\uparrow\rangle + |\text{☹}\rangle|\downarrow\rangle}{\sqrt{2}} \qquad (1)$$

where $|\text{☺}\rangle$ and $|\text{☹}\rangle$ refer to the states of a live and dead cat, and $|\downarrow\rangle$ and $|\uparrow\rangle$ refer to the internal states of an atom that has and has not radioactively decayed. This situation defies our sense of reality because we only observe live or dead cats, and we expect that cats are either alive or dead independent of our observation (*4*). Schrödinger's cat paradox is a classic illustration of the conflict between the existence of quantum superpositions and our real-world experience of observation and measurement.

Although superposition states such as Schrödinger's cat do not appear in the macroscopic world, there is great interest in the realization of "Schrödinger cat"–like states in mesoscopic systems, or systems that have both macroscopic and microscopic features. In this context, the "cat" is generalized to

The authors are in the Time and Frequency Division, MS 847, National Institute of Standards and Technology, Boulder, CO 80303, USA.

*To whom correspondence should be addressed.

represent a physical system whose attributes are normally associated with classical concepts, such as the distinguishable position of a particle (instead of the state of livelihood of a real cat). In this article, we report the creation of a mesoscopic "Schrödinger cat" state at the single atom level: An atom was prepared in a quantum superposition of two spatially separated but localized positions. In analogy to Schrödinger's original proposition given by Eq. 1, we created the following state:

$$\psi = \frac{|x_1\rangle|\uparrow\rangle + |x_2\rangle|\downarrow\rangle}{\sqrt{2}} \qquad (2)$$

where $|x_1\rangle$ and $|x_2\rangle$ denote classical-like wave packet states corresponding to separated spatial positions of the atom, and $|\downarrow\rangle$ and $|\uparrow\rangle$ refer to distinct internal electronic quantum states of the atom (5). The wave packets are separated by a mesoscopic distance of more than 80 nm, which is large compared with the size of the individual wave packets (≈7 nm) or the atomic dimension (≈0.1 nm).

Mesoscopic Schrödinger cats may provide an interesting testing ground for the controversial theory of quantum measurement (6). At the core of this historical issue is the question of the universality of quantum mechanics. The "Copenhagen interpretation" of Bohr (7) and Heisenberg (8) holds that the measuring apparatus always involves classical concepts, thus forcing a seemingly arbitrary division between the quantum and classical worlds. Einstein (2) on the other hand argued that for quantum mechanics to be complete, it should describe physical behavior at all scales. One practical approach toward resolving this controversy is the introduction of quantum decoherence, or the environmentally induced reduction of quantum superpositions into statistical mixtures and classical behavior (9). Decoherence is commonly interpreted as a way of quantifying the elusive boundary between classical and quantum worlds and almost always precludes the existence of macroscopic Schrödinger cat states, except at extremely short time scales (9, 10). The creation of mesoscopic Schrödinger cat states may allow controlled studies of quantum decoherence and the quantum-classical boundary. We note that quantum decoherence has received much interest lately because of its importance in proposals for quantum computation (11) and quantum cryptography (12).

Macroscopic superposition states of matter have been realized for electron (13), neutron (14), and atom (15) beam splitters, where these particles are split into superpositions of separated paths. The matter wave packets in these experiments spread in time because the particles are unbound. Spatially separated superpositions of electrons within atoms have been demonstrated by exciting electrons to Rydberg states with pulsed lasers (16). Here, the electron wave packet is also dispersive because of its anharmonic binding potential. There have been related proposals for the creation of macroscopic superposition states of vibration in molecules or crystals (17) and of electrical currents flowing in superconducting rings (18).

The appeal of creating a Schrödinger cat state in a harmonic oscillator is that wave packet dispersion can be negligible. The simple time evolution of a coherent harmonic oscillator wave packet preserves the separation of the superposition and aids in the visualization and interpretation of experiments. There have been several proposals to create mesoscopic Schrödinger cat states in a single mode of the electromagnetic field, which is formally equivalent to a harmonic oscillator. For instance, these states are expected to evolve from the amplitude dispersion of a laser beam propagating in an anharmonic Kerr medium (19). In cavity-quantum-electrodynamics, these states are predicted to emerge by driving a coherent state with a Jaynes-Cummings interaction to the point of collapse (20), by continuously pumping a single cavity mode with polarized two-level atoms (21), or by realizing a dispersive interaction between a single atom and a single cavity mode (22, 23). It has been proposed that Schrödinger cat states of a single harmonically bound atom can be created by driving the atom with a strong laser field and relying on a measurement to project the desired superposition state (24) or by optically pumping the atom to a "dark" state with multiple laser beams (25).

Experimental approach. In the present work, we create a Schrödinger cat state of the harmonic oscillator by forming a superposition of two coherent-state wave packets of a single trapped atom with a sequence of laser pulses. Each wave packet is correlated with a particular internal state of the atom. To analyze this state we apply an additional laser pulse to couple the internal states and then measure the resulting interference of the distinct wave packets (26, 27). The key features of our approach are that (i) we control the harmonic motion of the trapped atom to a high degree by exciting the motion from initial zero-point wave packets to coherent-state wave packets of well-defined amplitude and phase; (ii) we do not rely on a conditional measurement to project out the desired Schrödinger cat state; and (iii) wave packet dispersion of the atomic motion is negligible.

The experimental apparatus is described elsewhere (28, 29). A single $^9Be^+$ ion is confined in a coaxial-resonator radio frequency (RF)–ion trap (28) that provides harmonic oscillation frequencies of $(\omega_x, \omega_y, \omega_z)/2\pi \approx$ (11.2, 18.2, 29.8) MHz along the principal axes of the trap. We laser-cool the ion to the quantum ground state of motion (29) and then coherently manipulate its internal (electronic) and external (motional) state by applying pairs of off-resonant laser beams, which drive two-photon–stimulated Raman transitions (29, 30). As shown in Fig. 1A, the two internal states of interest are the stable $^2S_{1/2}(F = 2, m_F = -2)$ and $^2S_{1/2}(F = 1, m_F = -1)$ hyperfine ground states (denoted by $|\downarrow\rangle_i$ and $|\uparrow\rangle_i$, respectively), separated in frequency by $\omega_{HF}/2\pi \approx 1.250$ GHz. Here, F and m_F are quantum numbers representing the total internal angular momentum of the atom and its projection along a quantization axis. The Raman beams are detuned by $\Delta \approx -12$ GHz from the $^2P_{1/2}(F = 2, m_F = -2)$ excited state,

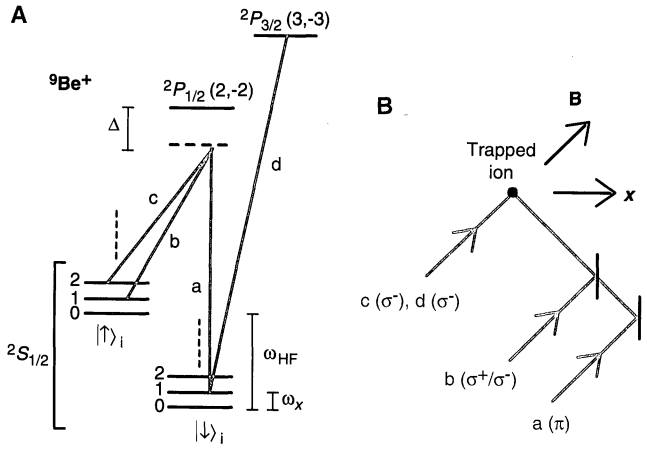

Fig. 1. (**A**) Electronic (internal) and motional (external) energy levels (not to scale) of the trapped $^9Be^+$ ion, coupled by the indicated laser beams a through d. The difference frequency of the "carrier" Raman beams a and b is set near $\omega_{HF}/2\pi \approx$ 1.250 GHz, providing a two-photon Raman coupling between the $^2S_{1/2}(F = 2, m_F = -2)$ and $^2S_{1/2}(F = 1, m_F = -1)$ hyperfine ground states (denoted by $|\downarrow\rangle_i$ and $|\uparrow\rangle_i$, respectively). The difference frequency of the "displacement" Raman beams b and c is set to $\omega_x/2\pi \approx 11.2$ MHz. This excites the motion of the ion to a coherent state $|\alpha e^{i\theta}\rangle_e$ from an initial zero-point state of motion $|0\rangle_e$ in the harmonic potential. Because of the polarization of beams b and c, they do not affect motion correlated with the $|\downarrow\rangle_i$ internal state. The three Raman beams (a, b, and c) are detuned $\Delta \approx -12$ GHz from the $^2P_{1/2}(F = 2, m_F = -2)$ excited state (radiative linewidth $\gamma/2\pi \approx 19.4$ MHz). Detection of the internal state is accomplished by first illuminating the ion with σ^--polarized "detection" beam d, which drives the cycling $^2S_{1/2}(F = 2, m_F = -2) \rightarrow {}^2P_{3/2}(F = 3, m_F = -3)$ transition, and then observing the scattered fluorescence. (**B**) Geometry of the three Raman laser beams a, b, and c, with polarizations indicated. The quantization axis defined by the applied magnetic field **B** is 45° from the *x* axis of the harmonic trap potential.

which acts as the virtual level, providing the Raman coupling. The external motional states are characterized by the quantized vibrational harmonic oscillator states $|n\rangle_e$ in the x dimension, separated in frequency by $\omega_x/2\pi \approx 11.2$ MHz.

When we tune the Raman beam difference frequency near ω_{HF} and apply the "carrier beams" a and b of Fig. 1, the ion experiences a coherent Rabi oscillation between the internal states $|\downarrow\rangle_i$ and $|\uparrow\rangle_i$. By adjusting the exposure time of the carrier beams, we can, for example, "flip" the internal state (a π-pulse, or one-half of a Rabi cycle) or "split-recombine" the internal state (a $\pi/2$-pulse, or one-fourth of a Rabi cycle). Transitions on the carrier do not significantly affect the state of motion, because beams a and b are copropagating. When we tune the Raman beam difference frequency near ω_x and apply the "displacement" beams b and c of Fig. 1, the effect is formally equivalent to applying the displacement operator to the state of motion (*30*). Alternatively, the displacement beams can be thought of as producing a "walking wave" pattern whose time-dependent dipole force resonantly excites the harmonic motion (*31*). This force promotes an initial zero-point state of motion $|0\rangle_e$ to a coherent state (*32*)

$$|\beta\rangle_e = \exp(-|\beta|^2/2)\,\Sigma_n\,\beta^n/(n!)^{1/2}|n\rangle_e \quad (3)$$

where $\beta = \alpha e^{i\theta}$ is a dimensionless complex number that represents the amplitude and phase of the motion in the harmonic potential (*33*). The probability distribution of vibrational levels in a coherent state is Poissonian with mean number of vibrational quanta $\langle n\rangle = \alpha^2$. The coherent state of motion is much like classical motion in a harmonic potential with amplitude $2\alpha x_0$, where $x_0 = (\hbar/2m\omega_x)^{1/2} = 7.1(1)$ nm is the root mean square Gaussian size of the oscillating wave packet, m is the mass of the ion, and $\hbar$ is Planck's constant divided by 2π (the number in parentheses is the standard error in the last digit).

The polarizations of the three Raman beams a, b, and c produce π, σ^+/σ^-, and σ^- couplings, respectively, with respect to a quantization axis defined by an applied 0.20-mT magnetic field, as indicated in Fig. 1B. As a result, the displacement beams (b and c) affect only the motional state correlated with the $|\uparrow\rangle_i$ internal state, because the σ^--polarized beam c cannot couple the internal state $|\downarrow\rangle_i$ to any virtual $^2P_{1/2}$ states (*34*). This selectivity of the displacement force provides quantum entanglement of the internal state with the external motional state. Although the motional state can be thought of as nearly classical, its entanglement with the internal atomic quantum levels precludes any type of semiclassical analysis.

Table 1. Raman beam pulse sequence for the generation of a Schrödinger cat state. The magnitude (phase) of the coherent state is controlled by the duration (phase) of the applied displacement beams in steps 2 and 4. The phases of internal state carrier operations in steps 1, 3, and 5 are relative to step 5. The states created after each step do not include overall phase factors, and the phase appearing in the final state is $\delta \equiv \mu - 2\nu + \pi$.

Step	Function	Approximate duration (μs)	Phase	State created (see Fig. 2) (initial state: $|\downarrow\rangle_i|0\rangle_e$)
1	Carrier $\pi/2$-pulse	0.5	μ	$[|\downarrow\rangle_i|0\rangle_e - ie^{-i\mu}|\uparrow\rangle_i|0\rangle_e]/\sqrt{2}$
2	Displacement	$\tau \approx 10.0$	$-\phi/2$	$[|\downarrow\rangle_i|0\rangle_e - ie^{-i\mu}|\uparrow\rangle_i|\alpha e^{-i\phi/2}\rangle_e]/\sqrt{2}$
3	Carrier π-pulse	1.0	ν	$[e^{i(\nu-\mu)}|\downarrow\rangle_i|\alpha e^{-i\phi/2}\rangle_e + ie^{-i\nu}|\uparrow\rangle_i|0\rangle_e]/\sqrt{2}$
4	Displacement	$\tau \approx 10.0$	$\phi/2$	$[e^{i(\nu-\mu)}|\downarrow\rangle_i|\alpha e^{-i\phi/2}\rangle_e + ie^{-i\nu}|\uparrow\rangle_i|\alpha e^{i\phi/2}\rangle_e]/\sqrt{2}$
5	Carrier $\pi/2$-pulse	0.5	0	$1/2|\downarrow\rangle_i[|\alpha e^{-i\phi/2}\rangle_e - e^{i\delta}|\alpha e^{i\phi/2}\rangle_e]$ $-i/2|\uparrow\rangle_i[|\alpha e^{-i\phi/2}\rangle_e + e^{i\delta}|\alpha e^{i\phi/2}\rangle_e]$

Each Raman beam contains ≈1 mW of power at ≈313 nm. This results in a two-photon Rabi frequency of $\Omega/2\pi \approx 250$ kHz for the copropagating Raman carrier beams a and b, or a π-pulse exposure time of about 1 μs. We apply the displacement Raman beams (b and c) to the ion in directions such that their wave vector difference $\delta\mathbf{k}$ points nearly along the x axis of the trap. Motion in the y or z dimensions is therefore highly insensitive to the displacement beams. When we apply the displacement beams to a zero-point wave packet (correlated with the $|\uparrow\rangle_i$ state) for time τ, we expect to create a coherent state of amplitude $\alpha = \eta\Omega_d\tau$. Here, $\eta = 0.205(5)$ is the Lamb-Dicke parameter (*30*) and $\Omega_d/2\pi \approx 300$ kHz is the coupling strength of the displacement beams. After each preparation cycle (described below), we detect which internal state ($|\downarrow\rangle_i$ or $|\uparrow\rangle_i$) the atom occupies independent of its state of motion. This is accomplished by applying a few microwatts of σ^--polarized light ("detection" beam d of Fig. 1A) resonant with the cycling $|\downarrow\rangle_i \rightarrow {}^2P_{3/2}(F = 3, m_F = -3)$ transition [radiative linewidth $\gamma/2\pi \approx 19.4$ MHz at wavelength (λ) ≈ 313 nm] and observing the resulting ion fluorescence. Because this radiation does not appreciably couple to the $|\uparrow\rangle_i$ state, the fluorescence reading is proportional to the probability $P_\downarrow$ the ion is in state $|\downarrow\rangle_i$. We collect on average about one photon per measurement cycle when the ion is in the $|\downarrow\rangle_i$ state (*29*).

Creation and detection of the Schrödinger cat state. The ion is first laser-cooled so that the $|\downarrow\rangle_i|n_x = 0\rangle_e$ state is occupied ≈95% of the time as described in (*29*). We then apply five sequential pulses of the Raman beams (the evolving state of the system is summarized in Table 1 and Fig. 2). In step 1, a $\pi/2$-pulse on the carrier splits the wave function into an equal superposition of states $|\downarrow\rangle_i|0\rangle_e$ and $|\uparrow\rangle_i|0\rangle_e$. In step 2, the displacement beams excite the motion correlated with the $|\uparrow\rangle_i$ component to a coherent state $|\alpha e^{-i\phi/2}\rangle_e$. In step 3, a π-pulse on the carrier swaps the internal states of the superposition. In step

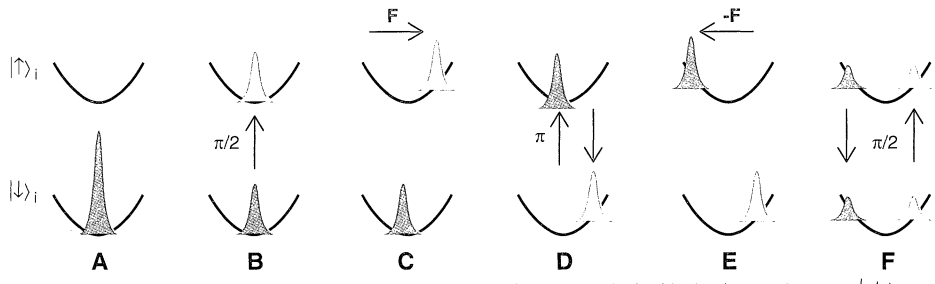

Fig. 2. Evolution of the position-space atomic wave packet entangled with the internal states $|\downarrow\rangle_i$ and $|\uparrow\rangle_i$ during creation of a Schrödinger cat state with $\alpha = 3$ and $\phi = \pi$ (see Table 1). The wave packets are snapshots in time, taken when the atom is at the extremum of motion in the harmonic trap (represented by the parabolas). The area of the wave packets corresponds to the probability of finding the atom in the given internal state. (**A**) The initial wave packet corresponds to the quantum ground state of motion after laser-cooling. (**B**) The wave packet is split after a $\pi/2$-pulse on the carrier. (**C**) The $|\uparrow\rangle_i$ wave packet is excited to a coherent state by the force **F** of the displacement beams. Note the force **F** acts only on the $|\uparrow\rangle_i$ wave packet, thereby entangling the internal and motional systems. (**D**) The $|\downarrow\rangle_i$ and $|\uparrow\rangle_i$ wave packets are exchanged following a π-pulse on the carrier. (**E**) The $|\uparrow\rangle_i$ wave packet is excited to a coherent state by the displacement beam force **−F**, which is out of phase with respect to the force in (C). The state shown in (E) corresponds most closely to Schrödinger's cat (Eqs. 1 and 2). (**F**) The $|\downarrow\rangle_i$ and $|\uparrow\rangle_i$ wave packets are finally combined after a $\pi/2$-pulse on the carrier.

4, the displacement beams excite the motion correlated with the $|\uparrow\rangle_i$ component to a second coherent state $|\alpha e^{i\phi/2}\rangle_c$. In step 5, a final $\pi/2$-pulse on the carrier combines the two coherent states. The relative phases of the above steps are determined by the phases of the RF difference frequencies of the Raman beams (*29*, *30*), which are easily controlled by phase-locking the RF sources.

The state created after step 4 is a superposition of two independent coherent states each correlated with an internal state of the ion, in the spirit of Schrödinger's original thought experiment (Eqs. 1 and 2). We verify this superposition by recombining the coherent wave packets in the final step 5. This creates the following entangled state:

$$|\Psi\rangle = |\downarrow\rangle_i|S_-\rangle_c - i|\uparrow\rangle_i|S_+\rangle_c$$

with

$$|S_\pm\rangle_c \equiv \frac{|\alpha e^{-i\phi/2}\rangle_c \pm e^{i\delta}|\alpha e^{i\phi/2}\rangle_c}{2} \quad (4)$$

For $\phi = \pi$ and $\delta = 0$, the states $|S_\pm\rangle_c$ (when properly normalized) are known as "even" and "odd" Schrödinger cats (*35*).

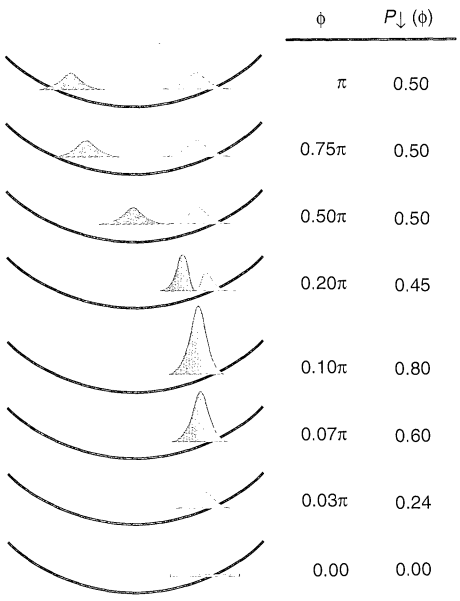

Fig. 3. Evolution of the position-space wave packet superposition correlated with the $|\downarrow\rangle_i$ internal state as the phase separation ϕ of the two coherent states is varied, for $\alpha = 3$ and $\delta = 0$. The expected signal $P_\downarrow(\phi)$ is the integrated area under these wave packets. Each trace is a snapshot in time, taken when one of the wave packets is at the rightmost turning point in the harmonic trap. The wave packets are maximally separated at $\phi = \pi$ [$P_\downarrow(\phi) \approx 1/2$], but they begin to overlap as ϕ gets smaller [$P_\downarrow(\phi)$ oscillates]. Finally, the wave packets destructively interfere at $\phi = 0$ [$P_\downarrow(\phi) = 0$]. This vanishing interference signal is a signature of an odd Schrödinger cat state associated with the $|\downarrow\rangle_i$ state, because $\delta = 0$. Probability conservation is ensured by a similar but constructive interference in the $|\uparrow\rangle_i$ state.

The relative populations of $|\downarrow\rangle_i$ and $|\uparrow\rangle_i$ depend on the motional phase difference ϕ between the two coherent wave packets because of the quantum interference between the two coherent states contained in $|S_\pm\rangle_c$. We directly measure this interference by detecting the probability $P_\downarrow(\phi)$ that the ion is in the $|\downarrow\rangle_i$ internal state for a given value of ϕ. We continuously repeat the experiment—cooling, state preparation, detection—while slowly sweeping the relative coherent state motional phase ϕ. Figure 3 depicts the expected position basis wave packet $|\langle x|S_-\rangle_c|^2$ correlated with the $|\downarrow\rangle_i$ internal state as a function of ϕ for $\delta = 0$ and $\alpha = 3$. The calculated wave packets in the figure are snapshots in time, as each part of the superposition oscillates in the harmonic trap. The measured signal $P_\downarrow(\phi)$ is just the integral of the complete $|\downarrow\rangle_i$ wave packet over space and is time-independent.

$$P_\downarrow(\phi) = \int_{-\infty}^{+\infty} |\langle x|S_-\rangle|^2 dx = \frac{1 - e^{-\alpha^2(1-\cos\phi)}\cos(\delta + \alpha^2\sin\phi)}{2} \quad (5)$$

The wave packets of the superposition are maximally separated in phase space for $\phi \approx \pm\pi$, where the signal is about 1/2 (for large α). However, as ϕ approaches 0, the wave packets of the superposition begin to overlap, finally interfering completely at $\phi = 0$. For large α, the signal $P_\downarrow(\phi)$ acquires oscillations near $\phi = 0$, with the width of the central interference fringe (in ϕ space) proportional to $1/\alpha^2$. If the two pieces of the wave packet are not phase-coherent or if the state is a statistical mixture (δ random between preparations) instead of a coherent superposition of wave packets, the signal would remain constant, $P_\downarrow(\phi) = 1/2$. We experimentally set the phase δ associated with the internal state superposition by blocking the displacement beams ($\alpha = 0$) and measuring $P_\downarrow = \sin^2(\delta/2)$.

Superpositions versus mixtures. In Fig. 4, we display the measured $P_\downarrow(\phi)$ for $\delta = 0$ and a few different values of the coherent state amplitude α, which is set by changing the duration τ of application of the displacement

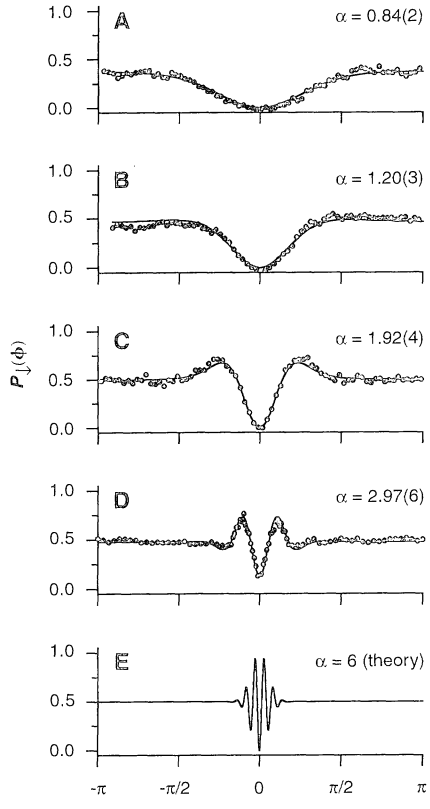

Fig. 4. Measured and fit interference signal $P_\downarrow(\phi)$ versus the phase difference ϕ of two coherent states for $\delta = 0$. Curves in (**A**) to (**D**) represent measurements for various values of τ (2, 3, 5, and 15 μs, respectively). As τ grows, the feature near $\phi = 0$ narrows. The lines are fits of the measurements to the parameter α (Eq. 4), yielding $\alpha = 0.84$, 1.20, 1.92, and 2.97, respectively. The fit in curve (D) includes a loss of contrast and represents a superposition of two $x_0 \approx 7$-nm wave packets with a maximum separation of $4\alpha x_0 \approx 80$ nm. Curve (**E**) is a theoretical plot for a pair of coherent states with $\alpha = 6$. Each data point in (A) to (D) represents an average of ≈4000 measurements, or 1 s of integration.

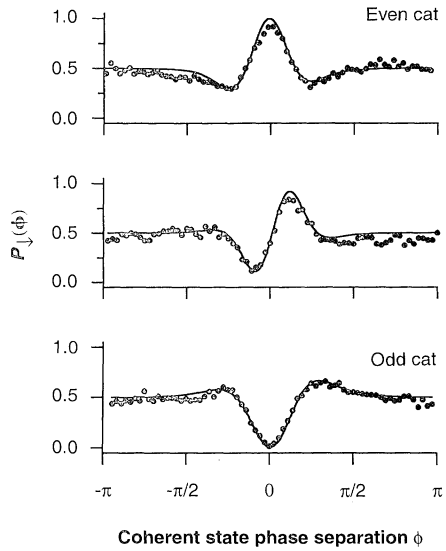

Fig. 5. Measured interference signal $P_\downarrow(\phi)$ for three values of δ ($\alpha \approx 1.5$). The top curve corresponds to $\delta = 1.03\pi$ (approximate even cat state correlated with $|\downarrow\rangle_i$ exhibiting constructive interference), the middle curve to $\delta = 0.48\pi$ [approximate "Yurke-Stoler" cat state (*19*)], and the bottom curve to $\delta = 0.06\pi$ (approximate odd cat state exhibiting destructive interference). Each data point represents an average of ≈4000 measurements, or 1 s of integration.

beams (steps 2 and 4 of Table 1). The presence of the interference feature near $\phi = 0$ verifies that we are producing superposition states instead of statistical mixtures, and the feature clearly narrows as α is increased. We have verified that the interference feature vanishes [$P_{\downarrow}(\phi) = 1/2$] when δ is randomized between preparations. In Fig. 5, we present $P_{\downarrow}(\phi)$ for three different values of the phase δ while fixing τ. The shape of the interference at $\phi \approx 0$ indicates the parity of the cat state at $\phi = \pm\pi$. Here, we see the transition from an even cat ($\delta \approx \pi$) to the Yurke-Stoler (*19*) cat ($\delta \approx \pi/2$) to an odd cat state ($\delta \approx 0$) correlated with the $|\downarrow\rangle_i$ state.

We extract the amplitude of the Schrödinger cat state by fitting the interference data to the parameter α appearing in Eq. 4. The extracted values of α agree with the independently measured value $\eta\Omega_d\tau$ for short displacement beam durations ($\tau \lesssim 10$ μs) (*36*). We measure coherent-state amplitudes as high as $\alpha \approx 2.97(6)$, corresponding to an average of $\langle n\rangle \approx 9$ vibrational quanta in the state of motion. This indicates a maximum spatial separation of $4\alpha x_0 = 83(3)$ nm, which is significantly larger than the single wave packet size of $x_0 = 7.1(1)$ nm. The individual wave packets are thus clearly separated in phase space.

For longer displacement beam durations ($\tau \gtrsim 10$ μs), the interference signal loses contrast, as evident in Fig. 4D. We believe this is partly due to fluctuations of the ion oscillation frequency ω_x, which causes the motional phase difference ϕ to fluctuate from measurement to measurement and wash out narrow interference features. The measured interference signal is sensitive to fluctuations of ω_x at a time scale that is longer than the time to create the cat ($\tau_c \approx \tau \approx 10$ μs) but shorter than the integrated measurement time (≈1 s per data point in Figs. 4 and 5). The observed loss of contrast indicates a phase fluctuation of $\delta\phi \approx 0.1$ rad, which would be consistent with a fractional ion oscillation frequency fluctuation of $\delta\omega_x/\omega_x \approx 10^{-4}$ in a ≈100-kHz bandwidth. Anharmonicities of the trap (*28*) are expected to contribute to a phase dispersion of only $\approx 10^{-6}$ rad during the creation of the cat.

Decoherence. When a Schrödinger cat consisting of two separated coherent states is coupled to a thermal reservoir, the superposition decays exponentially to a statistical mixture with a rate initially proportional to α^2, or the square of the separation of the wave packets (*9*, *10*, *27*). As the separation is made larger (more classical), the lifetime of the superposition shortens. This decoherence process underlies the reason quantum superpositions are not generally seen in the macroscopic world and also illustrates the experimental difficulty in preparing and maintaining even mesoscopic superpositions.

In the experiment, the quantum interference signal is only sensitive to decoherence during the period of time τ_c between the generation of the two coherent states (steps 2 and 4 of Table 1). This is because only the internal atomic state is detected, and once the second coherent state is produced (step 4), the internal and motional states do not interact, even if the motion equilibrates with an external reservoir. We therefore expect the interference signal (Eq. 4) to exhibit a contrast of $\exp(-\alpha^2\lambda\tau_c)$, where λ is the temperature-dependent relaxation rate to the thermal reservoir (*10*). The loss of contrast we observe may involve the onset of decoherence, although it is difficult to make a quantitative comparison because we do not know the spectrum and effective temperature of the supposed reservoir. We note that we have previously measured a heating rate of $\partial\langle n\rangle/\partial t \approx 10^3\ s^{-1}$ (*29*), but because the source of this heating is not understood at the present time, it is difficult to characterize its effect on decoherence.

The next step is to deliberately induce decoherence of the Schrödinger cat by coupling the system to "engineered" reservoirs during the interval τ_c. For instance, a uniform stochastic electric field can be applied, whose coupling to the ion could simulate a thermal reservoir at a controllable temperature. Alternatively, one can pulse the Raman beams and controllably allow spontaneous emission to occur during the interval τ_c [similar to stimulated Raman cooling (*29*)]. With this coupling, one can simulate thermal, zero-temperature, squeezed, and other reservoirs (*37*). By monitoring the contrast of the interference signal, it should then be possible to study the decoherence of the Schrödinger cat to these known reservoirs. The effects of decoherence might also be measured by mapping the complete density matrix of the Schrödinger cat state, as proposed in recent tomographic schemes (*38*).

We finally note that our technique for preparing Schrödinger cat superpositions of two coherent states in one dimension can easily be extended to create superpositions of more than two coherent states and superpositions in two and three dimensions. This technique may also be useful for the creation of superposition states of the collective motion of many trapped atoms.

REFERENCES AND NOTES

1. P. A. M. Dirac, *The Principles of Quantum Mechanics* (Clarendon, Oxford, ed. 4, 1984), p. 12.
2. A. Einstein, B. Podolsky, N. Rosen, *Phys. Rev.* **47**, 777 (1935).
3. E. Schrödinger, *Naturwissenschaften* **23**, 807 (1935); translation in (*6*).
4. Issues involving observation by the cat itself (by virtue of its consciousness) are beyond the scope of this article. For our purposes, the cat can be replaced, for example, by an object placed in a superposition of macroscopically separated positions.
5. In the literature, there is not universal agreement about the definition of the "cat" state. As opposed to the definition used in Eqs. 1 and 2 of this article, some authors prefer to define a Schrödinger cat state as $(|x_1\rangle + |x_2\rangle)/\sqrt{2}$, or a superposition of two classical-like states that are not correlated with the state of a second system. In the analysis of the state shown in Eq. 2, we in fact create the state corresponding to this alternate definition.
6. J. A. Wheeler and W. H. Zurek, Eds., *Quantum Theory and Measurement* (Princeton Univ. Press, Princeton, NJ, 1983).
7. N. Bohr, *Nature* **121**, 580 (1928); *Phys. Rev.* **48**, 696 (1935).
8. W. Heisenberg, *Z. Phys.* **43**, 172 (1927); translation in (*6*).
9. W. H. Zurek, *Phys. Today* **44**, 36 (October 1991).
10. D. F. Walls and G. J. Milburn, *Phys. Rev. A* **31**, 2403 (1985); C. M. Savage and D. F. Walls, *ibid.* **32**, 2316 (1985); M. J. Collett, *ibid.* **38**, 2233 (1988).
11. D. P. DiVincenzo, *Science* **270**, 255 (1995); I. L. Chuang, R. Laflamme, P. W. Shor, W. H. Zurek, *ibid.*, p. 1633.
12. C. H. Bennett, *Phys. Today* **48**, 24 (October, 1995).
13. L. Marton, J. Arol Simson, J. A. Suddeth, *Phys. Rev.* **90**, 490 (1954).
14. H. Maier-Leibnitz and T. Springer, *Z. Phys.* **167**, 368 (1962).
15. O. Carnal and J. Mlynek, *Phys. Rev. Lett.* **66**, 2689 (1991); D. W. Keith, C. R. Ekstrom, Q. A. Turchette, D. E. Pritchard, *ibid.*, p. 2693; M. Kasevich and S. Chu, *ibid.* **67**, 181 (1991); J. Lawall *et al.*, *ibid.* **75**, 4194 (1995).
16. L. D. Noordam, D. I. Duncan, T. F. Gallagher, *Phys. Rev. A* **45**, 4734 (1992); R. R. Jones, C. S. Raman, D. W. Schumacher, P. H. Bucksbaum, *Phys. Rev. Lett.* **71**, 2575 (1993); M. W. Noel and C. R. Stroud Jr., *ibid.* **75**, 1252 (1995).
17. J. Janszky, A.V. Vinogradov, T. Kobayashi, Z. Kis, *Phys. Rev. A* **50**, 1777 (1994); I. A. Walmsley and M. G. Raymer, *ibid.* **52**, 681 (1995).
18. A. J. Leggett and A. Garg, *Phys. Rev. Lett.* **54**, 857 (1985).
19. B. Yurke and D. Stoler, *ibid.* **57**, 13 (1986); *Phys. Rev. A* **35**, 4846 (1987); *ibid.* **36**, 1955 (1987).
20. S. J. D. Phoenix and P. L. Knight, *Ann. Phys.* **186**, 381 (1988); J. Gea-Banacloche, *Phys. Rev. Lett.* **65**, 3385 (1990); V. Bužek, H. Moya-Cessa, P. L. Knight, S. J. D. Phoenix, *Phys. Rev. A* **45**, 8190 (1992).
21. J. J. Slosser, P. Meystre, E. M. Wright, *Opt. Lett.* **15**, 233 (1990).
22. C. M. Savage, S. L. Braunstein, D. F. Walls, *ibid.*, p. 628.
23. M. Brune, S. Haroche, J. M. Raimond, L. Davidovich, N. Zagury, *Phys. Rev. A* **45**, 5193 (1992); S. Haroche and J. M. Raimond, in *Cavity Quantum Electrodynamics*, P. Berman, Ed. (Academic Press, New York, 1994), pp. 123–170.
24. J. F. Poyatos, J. I. Cirac, R. Blatt, P. Zoller, in preparation.
25. R. L. de Matos Filho and W. Vogel, *Phys. Rev. Lett.* **76**, 608 (1996).
26. L. Davidovich, A. Maali, M. Brune, J. M. Raimond, S. Haroche, *ibid.* **71**, 2360 (1993).
27. P. Goetsch, R. Graham, F. Haake, *Phys. Rev. A* **51**, 136 (1995).
28. S. R. Jefferts, C. Monroe, E. W. Bell, D. J. Wineland, *ibid.*, p. 3112.
29. C. Monroe *et al.*, *Phys. Rev. Lett.* **75**, 4011 (1995).
30. D. M. Meekhof, C. Monroe, B. E. King, W. M. Itano, D. J. Wineland, *ibid.* **76**, 1796 (1996).
31. D. J. Wineland *et al.*, in *Laser Manipulation of Atoms and Ions*, E. Arimondo, W. D. Phillips, F. Strumia, Eds. (North-Holland, Amsterdam, 1992), pp. 562–563.
32. R. J. Glauber, *Phys. Rev.* **131**, 2766 (1963); *ibid.*, p. 2529.
33. In the laboratory frame, the coherent-state parameter β has the periodic time dependence $\beta_L = \alpha e^{i(\theta - \omega t)}$, where ω is the frequency of the harmonic oscillator. Throughout the article, this time dependence is suppressed by working in an interaction frame where $\beta = \beta_L e^{i\omega t}$.
34. The effects of coupling to the $^2P_{3/2}$ excited state are small (detuning ≈ −210 GHz) and can be neglected here.
35. J. Peřina, *Quantum Statistics of Linear and Nonlinear Optical Phenomena* (Reidel, Dordrecht, 1984).

36. For large values of $\eta\Omega_d\tau$, we expect $\alpha(\tau)$ to saturate because of nonlinear correction factors that limit the amplitude of the coherent state and introduce amplitude squeezing [see (*31*) and W. Vogel and R. L. de Matos Filho, *Phys. Rev. A* **52**, 4214 (1995)]. For the experimental Lamb-Dicke parameter of ~0.2, these corrections are not significant for $\alpha \lesssim 5$.
37. J. F. Poyatos, J. I. Cirac, P. Zoller, in preparation.
38. D. T. Smithey, M. Beck, M. G. Raymer, A. Faridani, *Phys. Rev. Lett.* **70**, 1244 (1993); S. Wallentowitz and W. Vogel, *ibid.* **75**, 2932 (1995); J. I. Cirac and P. Zoller, in preparation.
39. We acknowledge key assistance from W. M. Itano, D. Leibfried, J. C. Bergquist, and J. Erickson and useful discussions with J. I. Cirac, P. Zoller, and D. Walls. We thank M. Young, S. Mechels, and D. Lee for critical comments on the manuscript. This work is supported by the U.S. Office of Naval Research and the U.S. Army Research Office.

2 January 1996; accepted 6 March 1996

The Whole Structure of the 13-Subunit Oxidized Cytochrome c Oxidase at 2.8 Å

Tomitake Tsukihara, Hiroshi Aoyama, Eiki Yamashita, Takashi Tomizaki, Hiroshi Yamaguchi, Kyoko Shinzawa-Itoh, Ryosuke Nakashima, Rieko Yaono, Shinya Yoshikawa*

The crystal structure of bovine heart cytochrome c oxidase at 2.8 Å resolution with an *R* value of 19.9 percent reveals 13 subunits, each different from the other, five phosphatidyl ethanolamines, three phosphatidyl glycerols and two cholates, two hemes A, and three copper, one magnesium, and one zinc. Of 3606 amino acid residues in the dimer, 3560 have been converged to a reasonable structure by refinement. A hydrogen-bonded system, including a propionate of a heme A (heme a), part of peptide backbone, and an imidazole ligand of Cu_A, could provide an electron transfer pathway between Cu_A and heme a. Two possible proton pathways for pumping, each spanning from the matrix to the cytosolic surfaces, were identified, including hydrogen bonds, internal cavities likely to contain water molecules, and structures that could form hydrogen bonds with small possible conformational change of amino acid side chains. Possible channels for chemical protons to produce H_2O, for removing the produced water, and for O_2, respectively, were identified.

Cytochrome c oxidase is the terminal oxidase of cell respiration, a process that reduces molecular oxygen to water with the electrons from cytochrome c, coupled to pumping protons from the matrix side of the mitochondrial membrane toward the cytosolic side (intermembrane space) (*1*). This enzyme contains two iron sites and two copper sites (Fe_a, Fe_{a3}, Cu_A, and Cu_B) in addition to zinc and magnesium sites (*1*). The protein moiety is composed of 13 different polypeptide subunits (*2*), three encoded by mitochondrial genes and ten by nuclear genes (*3*). Because of its physiological importance and the intriguing reaction catalyzed, this enzyme has been studied as one of the most important subjects in bioenergetics since its discovery (*4*). However, the difficulty in purification and crystallization of the large multicomponent membrane protein (*5*) has prevented determination of the crystal structure at an atomic resolution that could lead to the elucidation of the reaction mechanism.

Crystals of cytochrome c oxidase isolated from beef heart muscle have been obtained and the three-dimensional structure was solved at 2.8 Å resolution (*6*). These structures of metal sites confirmed earlier proposals that were based on mutagenesis and spectrophotometric data on, for example, ligand binding residues for hemes a and a_3 and Cu_B, the binuclear structure of Cu_A, and the relative locations of Fe_a, Fe_{a3}, and Cu_B. Unexpectedly, no direct bridging ligand from amino acids was observed between Fe_{a3} and Cu_B. We now describe the structure of the protein moiety and nonprotein constituents other than metals, which

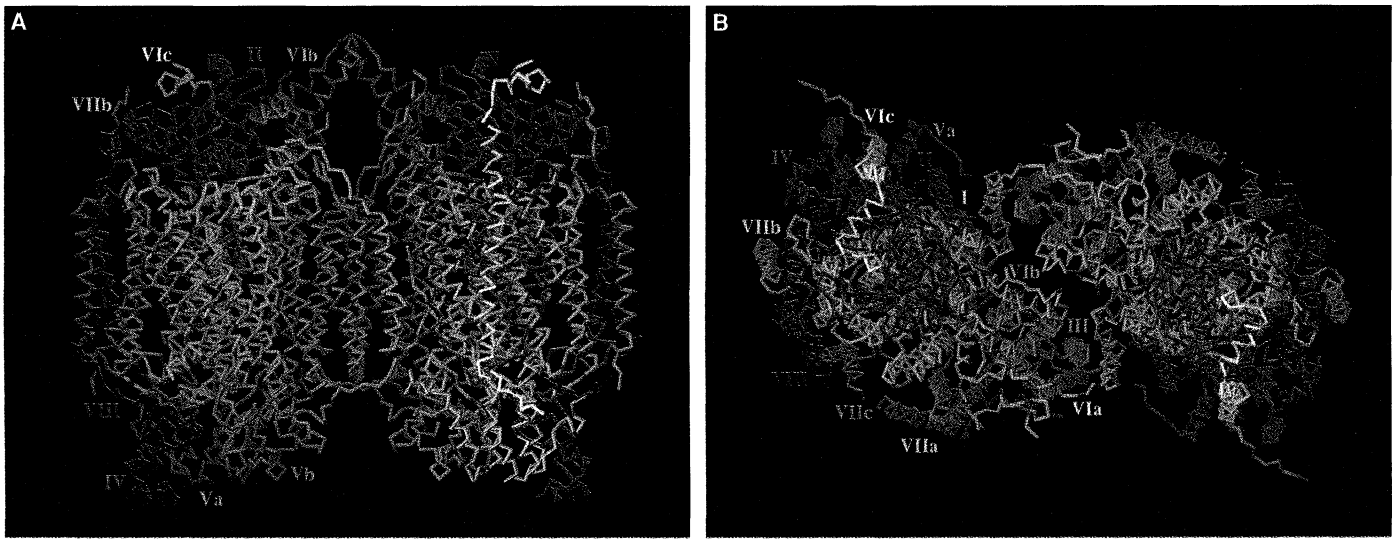

Fig. 1. The Cα-backbone trace of dimer of bovine heart cytochrome c oxidase. Crystallization, intensity data collection, phase determination and a procedure of density modification (*20*) have been described (*6*). Positional refinement followed by temperature factor refinement with program X-PLOR (*27*) reduced the *R* factor to 0.199 and the R_{free} to 0.252 at 2.8 Å resolution. The root mean square (rms) deviations from standard values of bond length and angles for the refined structure were 0.012 Å and 1.73°, respectively. Each monomer consists of 13 different subunits. (**A**) A view to the transmembrane surface and (**B**) a view from the cytosolic side. Both figures contain hemes a and a_3 and two Cu atoms of the Cu_A site (red). Each subunit has a different color with the subunit name in the color of the subunit (Brookhaven Protein Data Bank number, 1OCC).